

High-Speed Image Analysis and Filtered Imaging of Nested Hall Thruster Oscillations

IEPC-2015-285/ISTS-2015-b-285

*Presented at Joint Conference of 30th International Symposium on Space Technology and Science,
34th International Electric Propulsion Conference and 6th Nano-satellite Symposium
Hyogo-Kobe, Japan
July 4–10, 2015*

Ethan T. Dale* and Alec D. Gallimore†
University of Michigan, Ann Arbor, MI, 48109, USA

Hall Effect Thrusters (HET) are known to exhibit many high-speed oscillations that are indicative of thruster performance. Azimuthal ionization oscillations, called spokes, have been investigated extensively but the mechanisms governing their behavior are still poorly understood. Most experimentation has been done with single-channel Hall thrusters but evidence exists that a nested-channel Hall thruster experiences partial oscillation coupling between channels. This paper details the investigation of oscillations in various configurations of the X3, a 100-kW class three-channel nested Hall thruster. A technique of using optical filters to extract plasma properties from high-speed video is examined. Separately, coupling between channels was studied by imaging multiple thruster discharge channels at once. A Photron FASTCAM SA5 recording at 75,000 fps and equipped with thin dielectric filters for strong near-infrared Xe I emission lines was used to capture high-speed video of the discharge channel plasma. The recorded video for each thruster configuration was processed with radial averaging and azimuthal binning of the discharge channel light intensity, followed by 2D Fourier transforms to produce power spectral density curves for each mode. Phase delays between modes and relative fluctuation amplitudes were also calculated to quantify coupling. The filtered imaging work revealed that plasma parameters can be extracted at low speeds but degradation in emission model accuracy prevents it from being useful at high speeds. This paper also describes a preliminary summary of the coupling that is observed through the discharge current and light emission spectra. Barring pressure effects, breathing frequency convergence is observed consistently in two-channel operation but not uniformly in three-channel operation.

*Doctoral Candidate, Plasmadynamics and Electric Propulsion Laboratory, Department of Aerospace Engineering, 1919 Green Road, Room B107, Ann Arbor, MI 48109, etdale@umich.edu

†Arthur F. Thurnau Professor and Director, Plasmadynamics and Electric Propulsion Laboratory, Department of Aerospace Engineering, College of Engineering, 1320 Beal Avenue, Ann Arbor, MI 48109, alec.gallimore@umich.edu

Nomenclature

c	= speed of light in vacuum
f	= frequency
h	= Planck's constant
\tilde{I}	= root-mean-square discharge current amplitude
I_d	= discharge current
J_λ	= light intensity at a given wavelength
k_1^λ	= rate coefficient for ion collision excitation
k_{e0}^λ	= rate coefficient for electron collision excitation from the ground state
k_{em}^λ	= rate coefficient for electron collision excitation from a metastable state
k_{ep}^λ	= rate coefficient for electron collision excitation of state p
n_0	= neutral density
n_e	= electron density
n_m	= metastable density
\mathcal{P}_d	= discharge power
P	= branching fraction
P_{Xe}	= xenon-corrected chamber pressure
V_d	= discharge voltage
α	= ion-electron density ratio
λ	= atomic emission line wavelength
θ	= phase

I. Introduction

HALL Effect Thrusters are an increasingly attractive spacecraft propulsion solution for both satellite applications and interplanetary missions. Although the technology itself has been studied for decades, only recently have high-power thrusters (above 10 kW) been demonstrated. As these thrusters are designed for even higher power and begin to be incorporated into higher profile missions, the need to precisely understand their performance also grows. However, fulfilling it becomes difficult due to the limitations of ground testing. Vacuum chambers operating in the 10^{-5} to 10^{-6} Torr range are typically used to test these thrusters, although it is known that pressures are at least several orders of magnitude lower in most satellite applications¹ and will naturally be even lower for deep-space missions. Moreover, the presence of large conducting chamber walls during ground tests undeniably influences the electrical properties of the thruster.² These aspects of ground testing become problematic when evaluating thruster performance due to their effect on thruster instabilities. There is an extensive history of investigating high-speed Hall thruster instabilities, and these investigations have revealed that the performance of the thruster is a function of the type of oscillations its plasma exhibits.³ The nature of the oscillations can depend on a wide range of operating parameters, including background pressure, which may differ between ground tests and flight applications. A better understanding of the flight performance of modern Hall thrusters based on ground testing, then, is largely dependent on an understanding of high-speed thruster plasma oscillations.

This paper details an assessment of the application of xenon optical emission spectroscopy (OES) with a high-speed camera to studying HET oscillations. This entails an evaluation of whether OES can be performed with such a camera at all, and then whether the technique is applicable to the discharge channel plasma of a HET. In addition, the traditional optical techniques for examining these oscillations were applied to a three-channel nested Hall thruster to compare the behavior of the thruster between single-channel and multi-channel operation. In this way, the OES experiments present a unique spectroscopy implementation whereas the traditional imaging experiment is a well-developed technique applied to a novel thruster. Juxtaposed, the former is an example of new information that could be yielded with high-speed imaging, while the latter is an example of a new application for current high-speed imaging techniques.

II. Background and Theory

A. Hall Thruster Oscillations

Hall thrusters experience a wide variety of high-frequency oscillations that have been studied for nearly as long as the thrusters themselves.⁴ Instabilities in HETs can be exhibited as global oscillations (those where plasma properties vary only with time) and local oscillations (those where there is variation in time and space). Historically, four major types of instabilities have been identified: breathing, ionization spokes, transit-time oscillations, and drift spokes.⁴ The last two are well-described by theory^{5,6} and are generally considered to have little impact on performance, whereas the former have proven more difficult to grasp.

Although progress has been made in understanding the breathing and spoke modes in single-channel Hall thrusters, considerable experimental and theoretical work is still required for both. The breathing mode has classically been described as a predator-prey variation in ion and neutral densities,⁷ and some success was found by modeling them in this way.^{8,9} Barral and Ahedo identified several flaws with this model and proposed some corrections.¹⁰ More recent work by Hara and Sekerak has shown that, by accounting for electron energy perturbations within a predator-prey model, not only can breathing frequencies be reasonably predicted but instability criteria can also be determined.¹¹ Hara and Sekerak also analytically predicted regions of instability where the breathing mode becomes develops, and that these regions are traversed by changing operating parameters like magnetic field strength. At this time, more experimental work is needed to verify these models. Ionization spokes have not been described as successfully. Radial-axial codes have been used to reproduce the phenomenon¹² but a sound analytical model is lacking. Considerable effort has been expended on measuring spoke propagation with high-speed cameras, which has allowed empirical dispersion relations to be determined.¹³

The transition between modes and its ramifications on performance has also been described by Sekerak.³ It was found that for thrusters without magnetic shielding there exists a single transition between the breathing mode and spoke mode that coincides with a sharp decrease in thrust-to-power. For the case of varying magnetic field strength (but constant field topology), low field strengths are associated with the breathing mode, where discharge current is large and fluctuations in discharge current can be as great

as 100%. High field strengths are associated with the spoke mode, where discharge current is small and fluctuations are typically below 20%.³ Thrust generally stays constant between the modes but because the discharge current increases drastically for the breathing mode the thrust-to-power is higher in the spoke mode and peaks just before transitioning to the breathing mode. Work by Sekerak et al has shown that magnetically-shielded thrusters also experience a cathode mode in between the breathing and spoke regions, where local oscillations near the cathode are strong.¹⁴ Jorns et al argued that these cathode oscillations are driven by gradients in plasma density with a simple analytical model reproducing the shape and frequency of cathode oscillations observed experimentally.¹⁵

The oscillations exhibited by nested Hall thrusters have not been examined in detail to date. The two-channel 6-kW X2 thruster, built at the University of Michigan's Plasmadynamics and Electric Propulsion Laboratory (PEPL) and characterized by Liang,¹⁶ was studied with a high-speed camera by McDonald.¹⁷ No unusual behavior was observed for multi-channel operation, and general trends in spoke speed and strength with channel size were followed. The thruster exhibited both breathing and spokes simultaneously in all test conditions, and in only one condition was partial coupling detected, in which a spectral power peak from one channel appeared in the spectrum of the other. An analysis of the discharge current for the three-channel 100-kW class X3 thruster, built at PEPL and described preliminarily by Florenz,¹⁸ was also conducted. It was observed that the breathing frequency of different channels would tend to converge to a higher frequency when they were operated in unison.¹⁸

B. Xenon Optical Emission Spectroscopy

Optical emission spectroscopy, in which plasma parameters are related to the relative intensity of atomic emission lines due to spontaneous emission of plasma constituents, previously has been applied with some success to single-channel Hall thrusters operating on xenon.^{19–24} Initial efforts made use of models assuming corona equilibrium, where collisional excitation from the ground state is exactly balanced by spontaneous emission for all transitions of interest. Manzella applied such a model to measurements of a SPT-100 plume.¹⁹ He also assumed the plasma was in Boltzmann equilibrium but found that this assumption led to poor electron temperature predictions based on a comparison of the emission intensities as a function of energy to the underlying theory. Meezan interrogated a HET discharge channel with OES to examine high-speed oscillations.²⁰ This work made further use of the corona equilibrium assumption, and although oscillations could be meaningfully observed from optical emission line ratios, the electron temperatures computed from the model did not agree with those found with in situ electrostatic probes. This disagreement was attributed to a highly non-Maxwellian distribution, as expected for the discharge channel plasma.

Karabadzhak et al developed a collisional-radiative model that accounted for excitation from metastable states, greatly improving on the corona equilibrium model that preceded it.²¹ Considerable care was made in choosing emission lines related to states that were short-lived enough so as to have little collisional de-excitation but intense and distinct enough to allow for easy measurement. This model was improved in collaboration with Chiu and Dressler to become the Karabadzhak-Chiu-Dressler (KCD) model;²² this model was unique in relying more directly on experimental cross sections and in incorporating excitation by ion impact. Comparisons were made to plasma measurements far from a Thruster with Anode Layer (TAL) and eight-line least-squares extractions led to deviations of the modeled intensity ratios with experimental ratios of only about 28%. Dressler improved the model further by incorporating experimental emission cross sections reported by Jung and theoretical cross sections by Zatsarinny et al and Srivastava et al,²³ leading to deviations of only about 12% from far-field TAL measurements reported by Karabadzhak. However, few comparisons were made between the temperatures predicted by these models and those measured with other diagnostics, and so mainly the self-consistency of the models was evaluated.

More recently, the KCD model was applied by Gonzales et al to stroboscopically measure line ratios and predict time-resolved electron temperatures in the plume of a BHT-600 operated in the breathing mode.²⁴ In this case, a spectrometer was used in conjunction with a gated intensified charge-coupled device with custom timing electronics that allowed photon collection at specific phases with a periodic signal.

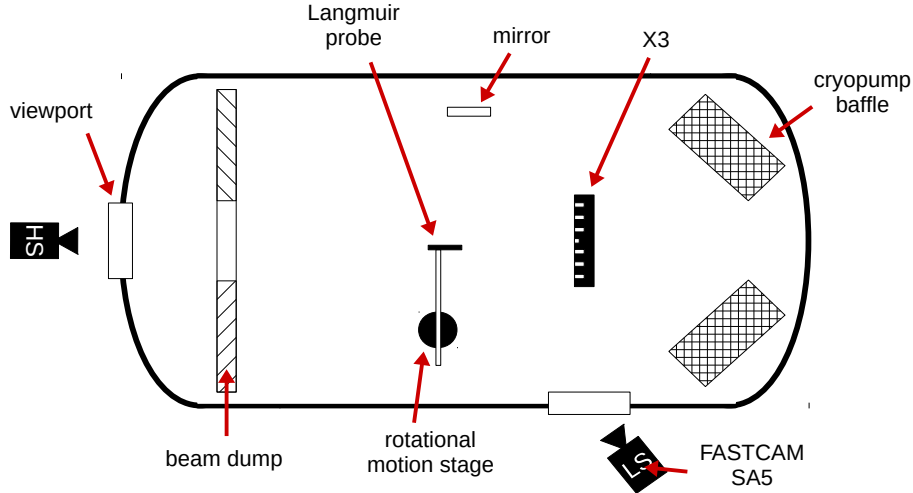


Figure 1. A schematic of the LVTF and the equipment used for the experiments discussed in this paper. The “HS” camera position was used for the high-speed imaging experiments, and the “LS” camera position was used for the low-speed filtered imaging experiment.

III. Experimental Setup

A. Facility and Thruster

Experiments were conducted in the Large Vacuum Test Facility (LVTF) located at PEPL. The LVTF is a stainless steel-clad cylindrical vacuum chamber that is 9 m long and 6 m in diameter. The chamber is equipped with a pair of 2000-CFM blowers and four 400-CFM mechanical pumps to reach rough vacuum, and a set of seven CVI TM-1200 LN₂-baffled re-entrant cryogenic pumps to reach high vacuum. The cryopumps collectively have a pumping speed of 500,000 L/s on air or 245,000 L/s on xenon, allowing base pressures on the order of 10^{-7} Torr. The chamber is equipped with two 29-cm diameter viewports, one located downstream of the thruster on the chamber axis, and the other on its side. The side viewport is nearly at the same chamber axial position as the thruster itself, approximately 3.6 m from the chamber hatch behind the thruster, and is roughly 6° above the chamber midplane. The layout of the chamber and the diagnostic equipment described later in this section are shown in Fig. 1.

The experiments detailed in this paper were conducted on the X3, a 100-kW class laboratory nested Hall thruster. A photograph of the X3 operating in the three-channel configuration is shown in Fig. 2. A description of the thruster design and its low-power performance was provided by Hall et al.²⁵ The thruster was operated at 300 V in single-channel, two-channel, and three-channel configurations, where the discharge power of each channel was kept approximately constant such that it operated at 30 kW in the three-channel case. A typical power achieved for each case is shown in Table 1, where the inner, middle, and outer channels are denoted as “I”, “M”, and “O” respectively, and cases where they are operated in unison are denoted by “+”. The inner channel is most comparable in size and power to the H6, a laboratory Hall thruster that has been extensively characterized and studied with high-speed diagnostics in both magnetically shielded and unshielded configurations.^{3,14}

The operating pressure of the X3 on xenon in these cases is shown in Table 1. The background pressure varied dramatically — across almost three orders of magnitude — between conditions, which made it hard to directly compare the operation of a given channel in single- and multi-channel configurations. This problem would be aggravated if the thruster was operated with a constant mass flow rate, in which case the thruster mass ingestion from ambient gas effectively leads to increased discharge current. To make comparisons more meaningful, the thruster was operated at constant channel power, as can be observed by summing the single-channel powers reported in Table 1. As a result, smaller mass flow rates were required for each channel when multiple channels were operated at once, but the discharge current for each remained the same as it was during single-channel operation. The background pressure was exceptionally high during the three-channel

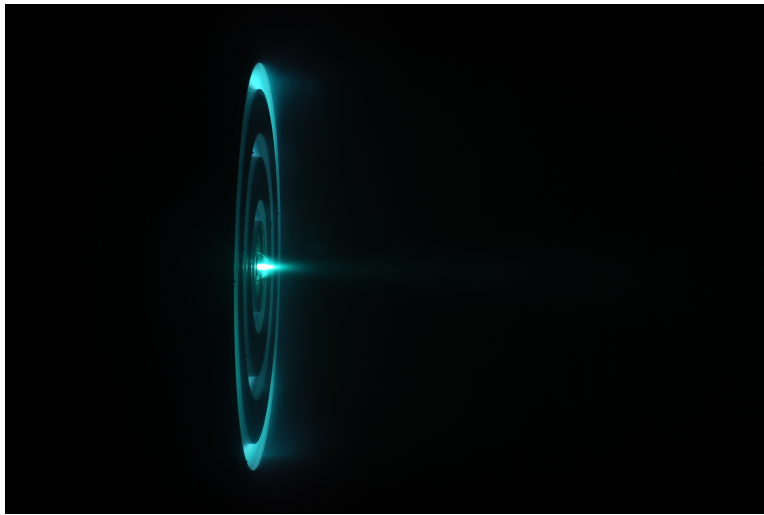


Figure 2. A photograph of the X3 operating at 30 kW with all three channels.

Table 1. The 30 kW operating conditions for each X3 configuration, as well as typical xenon-corrected operating pressures for each configuration, measured with a Varian 571 Bayard-Alpert ionization gauge.

Case	I_d (A)	V_d (V)	\mathcal{P}_d (kW)	P_{Xe} (Torr)
I	13.5	300	4.05	4.38×10^{-6}
M	31.4	300	9.42	9.60×10^{-6}
O	54.9	299	16.4	2.88×10^{-5}
I+M	13.4, 31.9	301, 300	13.6	1.31×10^{-5}
M+O	31.5, 54.8	299, 298	25.8	6.64×10^{-5}
I+O	13.3, 55.3	297, 299	20.5	3.85×10^{-5}
I+M+O	13.6, 32.3, 55	300, 300, 300	30.3	9.43×10^{-5}

configuration, well exceeding the recommended upper limit for performance evaluation.²⁶ Although this may have skewed thruster measurements for this case, it is assumed that the effect is at least somewhat mitigated by the constant power operation scheme.

B. High-Speed Discharge Current Analysis

One of the most easily implemented high-speed diagnostics to monitor the breathing mode is measurement of the thruster discharge current. A series of three Tektronix TCP303 current sensors and TCPA300 amplifiers was used to non-invasively measure AC-coupled anode current with a precision of 5 mA and DC accuracy within 1 A. The AC-coupled cathode current was also measured using a 0.1 V/A Ion Physics Corp. CM-10-H current transformer. A passive probe was chosen for measuring cathode current because it provided an effective means of monitoring thruster health during all phases of operation, including those during which discharge current transients could be strong enough to damage current sensors containing active electronics. Current signals were recorded with an Agilent DSO-X 3034A 200 MHz 8-bit oscilloscope. Acquisitions were performed at 5 MHz, spanned 200 ms, and relied on an external TTL signal for triggering.

The recorded current signals were Fourier transformed to reveal their spectral content. Because the discharge current is only sensitive to global oscillations, the most prominent peak in the power spectral density can usually be attributed to the breathing mode. With the memory constraints of the oscilloscope, the resulting spectra are noisy and the center frequency of the main spectral peak was identified using a Lorentzian fit.

The phase of each signal can also be estimated from the frequency domain data, although in this case the noisiness of the results made it difficult to determine strong phase features. Average phases from the real and imaginary components of the frequency-domain data over the half-maximum width of the spectral

peaks identified previously were calculated. It is important to note that this method of phase estimation is insensitive to transient phase changes — phase variation with time appears as noise in the phase spectrum. As a result, two signals may appear to have no phase delay when relying on the average phases, but in reality the signals were alternately out of phase over time. Additionally, phase delays are only meaningful if the signals under concern have the same frequency on average.

C. High-Speed Image Analysis

Both global and local oscillations can be detected with a high-speed camera by directly imaging the thruster discharge channel. A Photron FASTCAM SA5 operated at 75,000 fps was used for the experiments discussed in this paper. The FASTCAM has a CMOS sensor that can image 256×256 pixels at 75,000 fps. The camera acted as the trigger source for the oscilloscope used to record discharge current. The delay between the trigger signal and the first frame recorded by the camera was nominally $< 0.35 \mu\text{s}$. A Nikon Nikkor ED AF 80–200 mm zoom lens was used to image the thruster at a distance of 5 m using an $f/2.8$ aperture. Due to the size of the X3, the focal length was usually set close to 80 mm and even then only portions of the channels could be imaged. For plume imaging, the camera was at a distance of approximately 4 m from the plume axis. However, to image certain portions of the plume at less extreme angles, a 19×27 cm silvered glass mirror was used to redirect the optical path, lengthening it to nearly 6 m.

Once high-speed video was recorded, the images were processed frame by frame using a technique described by McDonald.²⁷ For imaging of the discharge channel, the process begins by algorithmically locating the discharge channel itself. In this experiment, however, only segments of the channel were in frame so its shape (approximated as an ellipse) and location had to be supplied manually. The mean image is subtracted from each frame such that only fluctuations are retained, and pixel intensities are averaged across azimuthal bins. The number of azimuthal bins is determined by the pixel size of the thruster image such that each bin encompasses at least an entire pixel in the shortest frame dimension. This binning is repeated for each frame, generating a 2D map of azimuthally-averaged pixel fluctuation intensities as a function of azimuthal position and time. This intensity map can succinctly describe oscillation features. Once global features, which appear as vertical bands in time-angle space, are removed by subtracting mean intensities at each time, spokes can easily be distinguished as diagonal features. The slope of these features, measured in degrees per time, can be used to estimate spoke speed given the thruster dimensions.

Similar to the high-speed discharge current analysis procedure, the discrete Fourier transform can be used to examine the frequency content of the high-speed video. In this case, however, the 2D transform is used so that separate spectra can be generated for local oscillations of different orders. For example, a zeroth order oscillation is the breathing mode, a first order oscillation is a single spoke (one bright region propagating around the channel), and a second order oscillation is a pair of spokes (two bright regions propagating around the channel). Due to the volume of data generated by the high-speed camera, even fewer samples are collected than with the oscilloscope, leading to slightly noisier spectra. As a result, Lorentzian fits are again used to determine the center frequency of the dominant feature in each spectrum, and half-maximum averaging is used to estimate the corresponding phase. Smearing of strong peaks to higher modes may occur due to spoke turbulence, but typically the strongest mode can be identified as that physically responsible for the oscillations at a given smeared frequency.

D. Xe I Optical Emission Model

A collisional-radiative emission model assumes that the intensity of light emitted at a certain transition wavelength is related to the rate at which particles excite to the upper energy state of that transition. In theory, this excitation comes from collisional excitation from lower states and cascade effects, where particles in higher states transition down to the given state. Additionally, radiation trapping – in which emitted photons are reabsorbed and excite particles – can contribute to the population of a given state either directly or by cascade. Light emission decreases due to diffusion losses and collisional de-excitation of the transition upper state. Since the latter requires considerable effort to model accurately and cross-section data for xenon is sparse, emission lines for states that are short-lived must be used. Diffusion can also be neglected for short-lived states, such that emission intensity is solely a function of excitation rate. However, excitation can be due to electron impact or ion impact, with the latter having an increasingly significant role as electron temperature decreases.²² Additionally, not only can the lower state for these excitations be the ground state but it may also be metastable states, which are long-lived enough to experience particle

collisions before spontaneous emission. Ignoring metastables as in the corona equilibrium assumption greatly simplifies the model, but unfortunately metastables have a non-negligible influence on emission either through excitation or metastable diffusion losses, as the success of the KCD model attests.²²

The KCD model can be described in terms of its collisional-radiative model formulation as well as the lines to which the model is tailored. As for the former, the KCD model fundamentally assumes that the intensity of light emitted at a certain wavelength J_λ is a function of the particle excitation rates from lower states due to electron collisions k_{ep}^λ and from the ground state due to ion collisions k_1^λ , assuming optical thinness. Naturally, the electron collision term depends on the target state density n_p and the electron density n_e , while the ion collision term depends on the neutral density n_0 and the ion density n_i . This is shown as Eq. 1. For now, the emission lines of interest are associated with neutral excited states, although the exact states themselves do not need to be determined yet. It is assumed here that the transition of interest that emits at wavelength λ is short-lived enough such that all depopulation is by spontaneous emission. Additionally, the formulation presented here only includes excitation from singly-ionized particles since Karabadzah et al noted that the influence of the doubly-charged ions is small, even though their formulation retained the doubly-charged ion terms.²²

$$J_\lambda = \frac{hc}{4\pi\lambda} n_0 n_e \left(\sum_p \frac{n_p}{n_0} k_{ep}^\lambda + \frac{n_i}{n_e} k_1^\lambda \right) \quad (1)$$

If it is assumed that most ions are energized to the thruster discharge voltage, the excitation rate due to ion collisions can be simplified. Additionally, if quasi-neutrality is assumed such that the ratio of singly-charged ion density and electron density α is constant, Eq. (2) results. Notice that the first term in Eq. 1 has been replaced with a ground state term and a metastable state term, where the latter depends on the electron collision excitation rate from the metastable state k_{em}^λ and the metastable state density n_m .

$$J_\lambda = \frac{hc}{4\pi\lambda} n_0 n_e \left(k_{e0}^\lambda + \frac{n_m}{n_0} k_{em}^\lambda + \alpha k_1^\lambda \right) \quad (2)$$

Since comprehensive cross sections for Xe I metastables are rare, a specific set of emission lines had to be defined to advance Eq. (2) further. Several near-infrared (NIR) lines associated with the Xe I $2p_i$ (Paschen notation) states are very intense for HET plasmas, and so the KCD model uses the emission lines associated with transitions down from these states. It was noted that three of these lines, $2p_1$, $2p_3$, and $2p_5$, are only weakly coupled to nearby metastable states and instead de-excite to the $1s_2$ and $1s_4$ resonant states. This allows these states to be modeled without considering metastable densities or cross sections, eliminating the middle term in Eqn. (2). However, the strongest $2p_i$ lines are dipole-coupled to metastable states and therefore depend on metastable properties. The KCD model approximates metastable density by forming an equilibrium rate equation in which the metastable state is populated by spontaneous emission from all states that de-excite to the metastable state and is depopulated by collisional de-excitation and diffusion. Diffusion losses can be shown to be insignificant compared to collisional de-excitation for all but very low temperatures.²² The rate of collisional de-excitation is estimated from the collisional excitation cross sections out of the metastable state, weighted by the branching ratio P of the resulting upper state to nearby states that resonate to ground. That is, de-excitation of the metastable state is the average rate of collisional excitation such that a particle cannot enter the metastable state without re-exciting from the ground state. With these approximations, the ratio of metastable density to ground state neutral density is given by Eq. (3).

$$\frac{n_m}{n_0} = \frac{\sum_i (k_{e0}^i + \alpha k_1^i)}{\sum_i P_i k_{em}^i} \quad (3)$$

The rate coefficient for excitation from the metastable state is approximated as proportional to the degeneracy of the higher energy state scaled by the branching probability for the $2p_i$ end state to the metastable state.²² The constant of proportionality does not need to be determined since the metastable density ratio is also proportional to degeneracy through the k_{em}^i term.

Work by Dressler et al removed the metastable approximations of the KCD model by applying a combination of experimental cross sections from Jung²⁸ and theoretical cross sections produced with the Breit-Pauli B-Spline R-matrix (BSR) method and relativistic distorted wave (RDW) method. The same equilibrium rate equation was used to determine metastable density ratio, except the relevant experimental or theoretical rate

coefficients were used instead of weighted rate coefficients. Likewise, the metastable rate coefficient did not need to be estimated from the degeneracy but could be directly calculated from experimental and theoretical cross-sections. The resulting model, which showed better eight-line extractions to Karabadzhak et al’s TAL data than the KCD model, is called the BSR-RDW-Jung model.

Once the model is formulated, the manner in which it will be compared to experimental data must also be considered. The most thorough method is to perform a least-squares fit of normalized intensities as a function of temperature for all modeled emission lines. For the KCD and BSR-RDW-Jung models, this involves extracting the temperature corresponding to the best fit for eight emission lines normalized to each other compared to the experimental normalized intensities. However, as few as two intensities is sufficient for comparison with the model, since normalizing intensities is only needed to eliminate the density dependence of J_λ and obviate the determination of relative spectral response of the optical system. In some cases, using fewer lines may be preferable as a subset of the modeled emission lines may have greater accuracy than the entire eight-line extraction under certain circumstances. Dressler noted this for the 834 and 828 nm NIR lines using the KCD model.²³

To make use of these models with a high-speed camera, optical filters must be employed to limit the range of wavelengths detected by the camera. If the spectral response of the filters is known precisely enough, the model intensities can be composed to estimate the relative intensity transmitted by a given filter. As a result, a minimum of two filters can be used estimate electron temperature with the previously described models. For the experiments described in this paper, 820-nm and 830-nm Fabry-Perot thin dielectric stack filters were used, each 25 mm in diameter and with a 10-nm full-width half-maximum (FWHM). The spectral response of the camera-filter system for unit emissions at a few modeled wavelengths is shown in Fig. 3; this response curve accounts for sensor response, lens transmittance, filter transmittance, and natural and collisional line broadening. Note that the range of wavelengths for the spectral response is fairly limited but the logarithmic shape of the response curve suggests that this should not greatly affect the performance of the model since the spectral response varies over several orders of magnitude. Also included in Fig. 3 is the variation in emission intensity with temperature according to the KCD model. This plot shows that with increasing temperature all line intensities increase rapidly, peak, and then slowly decrease. The high temperature accuracy of the model may be poor, though the observed trend does agree with the shape of the relevant excitation cross sections. These two plots can be combined to yield Fig. 4, which shows the ratio of filter intensities as a function of effective Maxwellian electron temperature. The filter ratio is a unique function of temperature using either the KCD or BSR-RDW-Jung model, which is necessary for the estimation of electron temperature from emitted light but not guaranteed when composing intensities that are individually unique functions of temperature, as was done for this experiment.

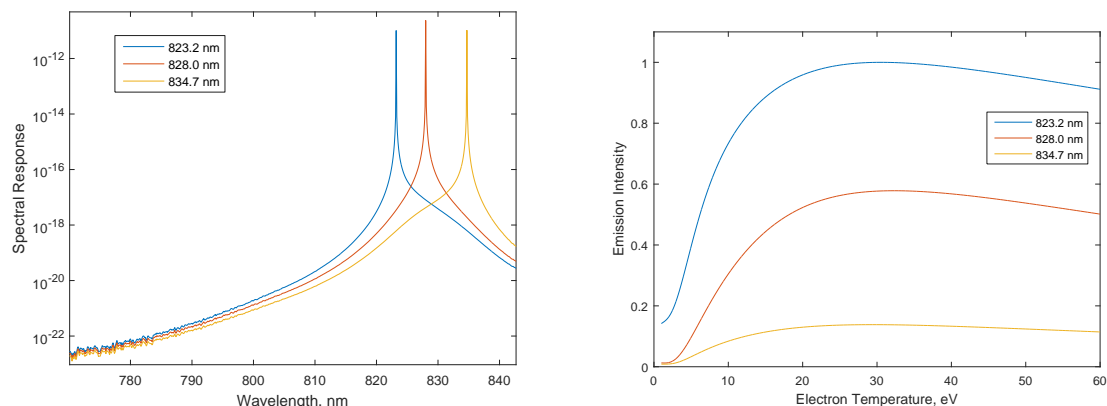


Figure 3. The spectral response of the camera, filter, and lens system for unit emissions near 820 and 830 nm (left), and the normalized emission intensity for the same lines as a function of temperature (right).

Optical emission plume measurements were compared to Langmuir probe data acquired within the field of view of the camera. A dual cylindrical Langmuir probe with a 10 mm by 0.6 mm diameter tungsten tip was located 1.6 m downstream of the thruster, on thruster centerline and aligned axially with the thruster. The probe was sinusoidally swept at 10 Hz from -20 to 50 V using an Agilent 33220A arbitrary waveform generator and a Krohn-Hite 7500 amplifier, and the collected current was measured by comparing voltage across two

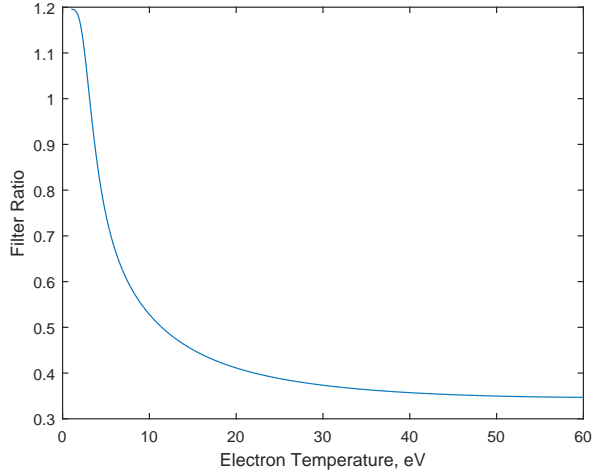


Figure 4. The filter ratio according to the KCD model is a unique function of electron temperature, allowing it to be used for diagnostic purposes. The slope approaches zero as temperature increases, meaning that the model is less effective in that limit.

low-inductance resistors matched to within 0.1Ω via trim potentiometer. Although having a dual probe is not necessary at such low sweep rates, it was included to allow for faster sweeping if desired. Voltages were acquired with a pair of AlazarTech ATS9462 16-bit, 180 MHz PCIe digitizer cards. Approximately twenty I-V traces were collected per acquisition and averaged within 0.1 V bins to mitigate signal noise.

There are several immediately apparent limitations to using a high-speed camera for OES. Two cameras recording in unison could theoretically be used to collect time-resolved filter ratios, which could then yield time-resolved electron temperature measurements. It is more practical, however, for a single camera to be used repeatedly with different filters to collect time-resolved intensities. Then either the temporal or spatial periodicity of the signal can be used to correlate the separate measurements and determine time-resolved filter ratios. Naturally, this latter option either requires that the thruster is experiencing global oscillations or it necessitates considerable post-processing to isolate periodic spatial features like spokes. Additionally, given that the motivation for using a high-speed camera for emission spectroscopy is its capacity to image the entire thruster discharge channel at once, it should be noted that the existing collisional-radiative models are tailored for low-temperature regions of the thruster plasma. If high temperature regions like the discharge channel are considered, only a few of the eight lines in the KCD and BSR-RDW-Jung models are sufficiently short-lived to be useful. A further challenge is that additional emission lines may become measurable at high temperatures, such as an Xe II line near the 834 nm Xe I line.²³ When using filters and relying on precise knowledge of the location of each major emission line for filter intensity composition, these intruding lines will degrade the accuracy of the model. The error introduced by these intruding lines and the degradation of the model at high temperature was investigated as part of the experiments described in this paper in an attempt to characterize the deficiencies in a discharge channel OES implementation.

IV. Results

A. Low-Speed Filtered Imaging

To evaluate the suitability of the FASTCAM for emission spectroscopy, time-averaged measurements of the plume were made. This condition is well-suited to the KCD and BSR-RDW-Jung models, and by comparing to Langmuir probe measurements, should be an excellent benchmark for FASTCAM OES. The unfiltered images of the inner channel baking out near 4 kW are shown in Fig. 5, captured by the FASTCAM at 60 fps without using a mirror. Also included are the 820-nm and 830-nm filtered images acquired sequentially over the course of several minutes. These images show that the Langmuir probe and its stand were within the field of view of the camera. In this configuration, the camera was rotated 28° about the vertical axis and 29° about the chamber axis, so these raw images contain some angular distortion that could be avoided

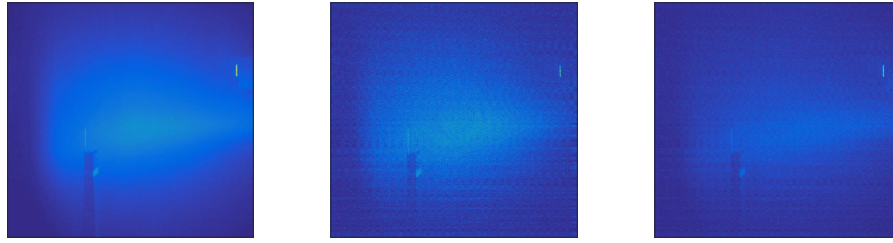


Figure 5. Images of the X3 inner channel plume operating during bakeout near 4 kW, captured by the FASTCAM SA5 unfiltered (left), filtered around 820 nm (middle), and filtered around 830 nm (right). The graininess of each image is an indication of its intensity, but otherwise the intensity is scaled during plotting.

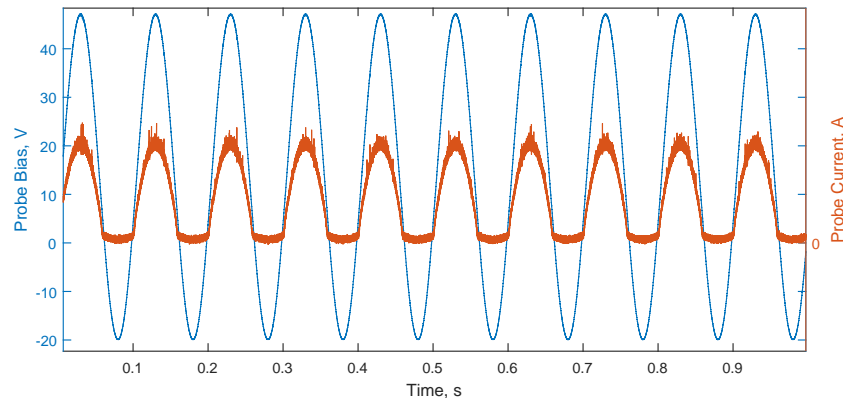


Figure 6. A sample of the Langmuir probe data acquired over 1 s, encompassing roughly ten sweep cycles or twenty I-V curves. Note the probe bias did not reach the waveform generator limits due to voltage drops across the shunt resistors. There is noticeable noise in each trace, and the low-current regions of each I-V curve appear to consist entirely of noise.

with a mirror. Pixel intensities normalized to bit depth at this condition averaged 0.047, 0.0033, and 0.0041 for the three cases respectively, and the average root-mean-square (RMS) noise normalized to the bit depth over 100 frames was 0.0022, 0.0015, and 0.0016. This indicates that, without taking extra measures to reduce sensor noise, the signal is fairly noisy and may require smoothing to account for isolated noisy pixels. As expected, the filters appear to cut out a considerable amount of light, although it is likely that the small filter size (encompassing only 8% to 9% of the lens area) is blocking out a significant portion of incoming light.

A Langmuir probe acquisition made just prior to the FASTCAM imaging is shown in Fig. 6. With the current sensing method employed here, the voltage range for the DAQ cards was such that the ion saturation current of the Langmuir probe was below the noise floor of the cards. Additionally, the collected current was a noisy trace to trace, indicating that considerable averaging is required.

B. High-Speed Filtered Imaging

As a proof of concept, the FASTCAM was also used to capture filtered video of the X3 inner channel during bakeout near 4 kW while in the single-channel configuration. Fig. 7 shows the unfiltered and filtered raw images captured by the camera at 75,000 fps. These images show that nearly the entire discharge channel could be imaged and the signal was strong even when filtered. Note here that the graininess of the filtered images indicates that the sensed intensities are much lower than for the plume images due to the much higher shutter speed. The mean pixel intensities normalized to the bit depth are 0.016, 0.0011, and 0.0010 for the unfiltered, 820-nm filtered, and 830-nm filtered images, respectively. In this case, the pixel-by-pixel discharge channel intensity RMS is not necessarily indicative of noise as it was for the time-averaged plume data, but the noise in the rest of the image can be used as such an indicator. In this case, the sensor dark

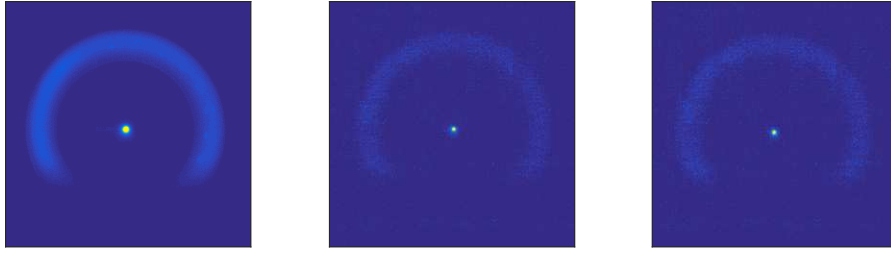


Figure 7. Time-averaged images of the X3 inner channel during bakeout near 4 kW, captured by the FASTCAM SA5 unfiltered (left), filtered around 820 nm (middle), and filtered around 830 nm (right). Note that there is considerable loss in image intensity when filters are added, although the channel is still discernible and the cathode is still particularly brilliant. Although only 204° of the channel was visible, the azimuthal bin size was small enough to discern several spatial modes with the 2D discrete Fourier transform.

noise pixel intensity normalized to the bit depth over 1000 frames was about 0.00078, 0.00068, and 0.00063. On average, then, a meaningful filtered signal is sensed, but only after further analysis in Section V will the impact of noise on the time-resolved signal become clear.

C. Discharge Channel Oscillations

An inspection of the discharge current signals for all configurations of the 300 V operating condition examined in this paper leads to the conclusion that the breathing mode was likely dominant in all cases. Fig. 8 is an example of the intensity surface and discharge current during breathing, in this case for the operation of the middle channel alone at 9 kW. The discharge current is strongly periodic, and the intensity surface shows defined vertical (global) features.

For two-channel operation, the breathing discharge current fluctuation amplitude was sometimes greater in the smaller of the two channels, and other times greater in the larger of the two. Fig. 9 shows an example of the former for the inner and middle two-channel configuration at 14 kW, as well as an example of the latter for the inner and outer two-channel configuration at 21 kW. The configuration with the inner and middle channel operating together appears to have much weaker breathing than most cases like Fig. 8, such that it may be an example of a transitional case where the thruster is between modes. The analysis in Section V will examine this case in greater detail.

Perhaps the only condition where breathing was not clear for all channels was the three-channel configuration at 30 kW. The discharge current for all three channels and the cathode in this configuration is presented in Fig. 10. In this case, breathing is apparent for the cathode, middle channel, and outer channel, but a more erratic discharge current is exhibited by the inner channel.

V. Analysis and Discussion

A. Low-Speed Filtered Imaging

The binned and averaged I-V curve and logarithmic I-V curve based on the acquisition shown in Fig. 6 is displayed in Fig. 11. As mentioned previously, noise in the DAQ card prevented the probe current from ever diminishing to zero on average, so there is uncertainty added to the calculated temperature due to the unknown ion saturation current. However, as the logarithmic electron current shows, a very linear electron retarding region is apparent. Fitting a line to this region yields an estimate of electron temperature of 3.76 ± 0.48 eV assuming a Maxwellian energy distribution.

Figure 12 shows the raw filter ratio map and the angle-corrected temperature map using the KCD model, spatially binned and averaged to 8×8 mm squares. The KCD model was used here as it gave better performance than the BSR-RDW-Jung model. The probe was located in the lower left corner of the maps, and averaging 100 pixel temperatures around that edge yields a temperature of 2.99 ± 0.03 eV. The uncertainty on this temperature is due only to noise, as the systematic uncertainty of the camera measurements are hard to determine, and the uncertainty related to the fidelity of the OES model is likewise difficult to quantify.

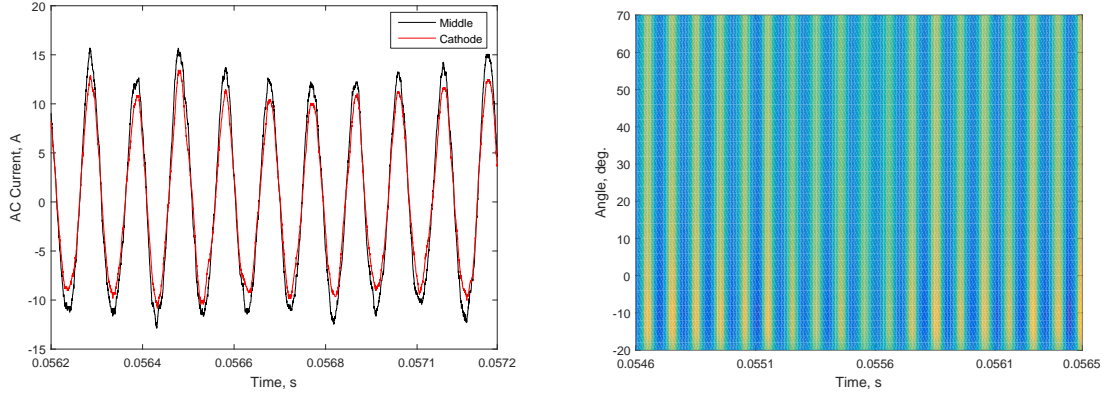


Figure 8. An example of the breathing mode for the X3 middle channel operating at 9 kW, as an intensity map encompassing 90° of the channel (right) and as discharge current (left). Note that the middle channel current tracks very closely with the cathode current, as expected for a single-channel operation.

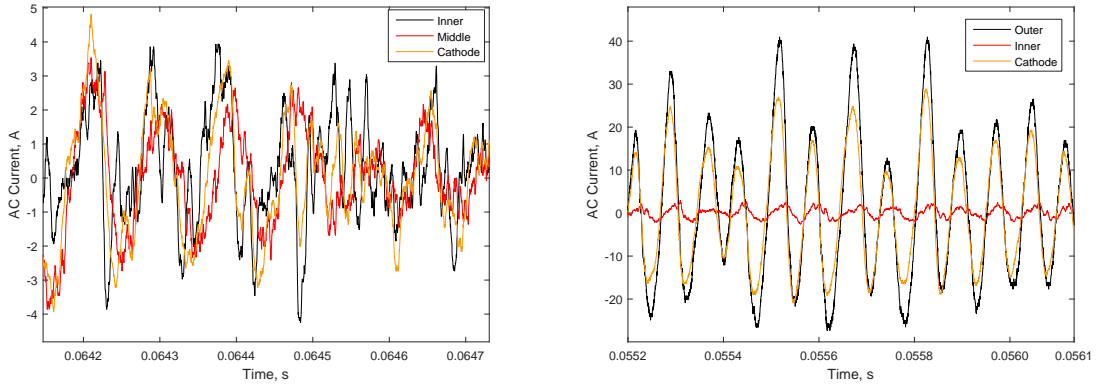


Figure 9. An example of a smaller channel having slightly higher current fluctuations than a bigger channel (left) and the opposite (right). The former case shows the inner and middle channels operating together at a total power of 14 kW. In this case the breathing appears very weak, as all AC current signals appear noisy and have low amplitude. The latter case shows the inner and outer channels operating together at a total power of 21 kW. In this case, breathing is very strong, as the clear sinusoidal outer channel AC current signal indicates. The inner channel still appears noisy but breathing oscillations are easily identifiable.

In any case, there appears to be fair agreement between the two diagnostics, with an error of 20.4%. The uncertainty of both measurements may be large enough (relative to the actual temperatures measured) that the agreement is not particularly impressive; in fact, the uncertainty of the Langmuir probe measurement alone is at least 12.8% of the computed temperature. Further, this only shows agreement for very low temperatures (a small region of the imaged area), which is supposedly the ideal case for the KCD model; again, this means that the agreement is not surprising. The trend of increasing temperature toward the right (toward the thruster) is reasonable. On the other hand, the high temperatures at the rightmost extent of the map do not seem plausible. By examining the raw temperature map, shown in Fig. 13, it becomes clear where these high temperatures originate. The data is fairly sparse close to the thruster, and there are a few data points in that region with erroneously high temperatures according to the OES model. It is likely that these high-temperature points — corresponding to very low filter ratios — are a result of sensor noise, defective pixels, or residual charge in the sensor electronics between frames. In general, the sparsity of data is a result of pixels with abnormally high filter ratios, again potentially due to sensor noise or defects.

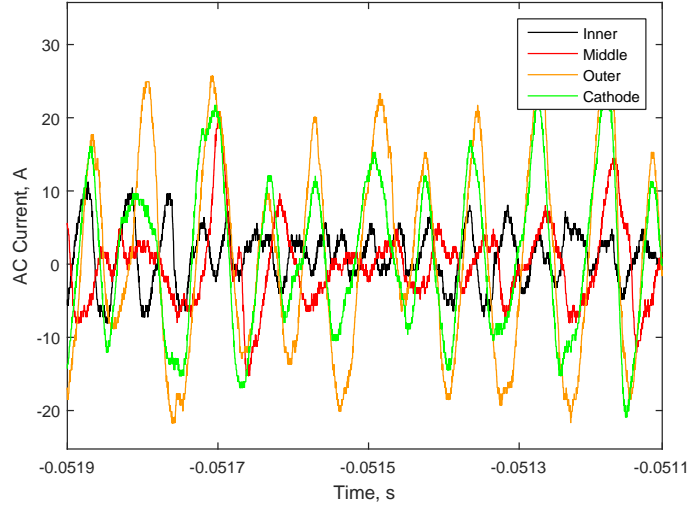


Figure 10. The cathode current and anode current for all three channels operating in unison at 30 kW. The outer channel and cathode appear to track very closely, and middle channel seems to have a phase delay with them. The inner channel appears very noisy and clearly does not follow the shape of the other signals.

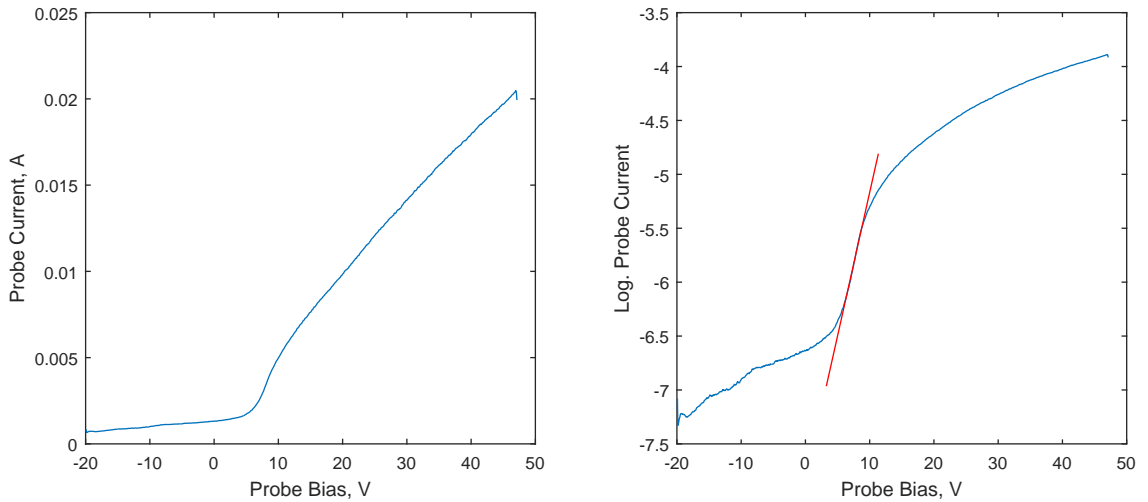


Figure 11. The probe current as a function of applied voltage after 0.1-V binning (left), and logarithmic electron current as a function of applied voltage after the same binning (right). The curves appear very smooth except toward low voltages, where the measured signal was mostly DAQ noise. Slight deviations at the ends of either curve are due to the binning algorithm, and have no bearing on the temperatures determined from these curves. The linear fit to calculate temperature is shown in red.

B. High-Speed Filtered Imaging

The unfiltered DC-coupled pixel intensity as a function of time and discharge channel azimuthal position was produced using the high-speed image analysis techniques described in Section III, and is shown in Fig. 14. Neither the breathing mode nor spoke mode was strong in this operating condition, although there is some spoke-like feature from 0° to 20° . Although the nominal 4 kW operating condition for the X3 inner channel demonstrated strong breathing, this experiment was conducted during bakeout for the condition, during which the high-speed behavior of the thruster is anticipated to be erratic. This represents one of the worst possible conditions for sequential filtered imaging, as was implemented in this experiment. However, the spectrum for the entire channel as shown in Fig. 15 indicates that there is still weak breathing near 5 kHz.

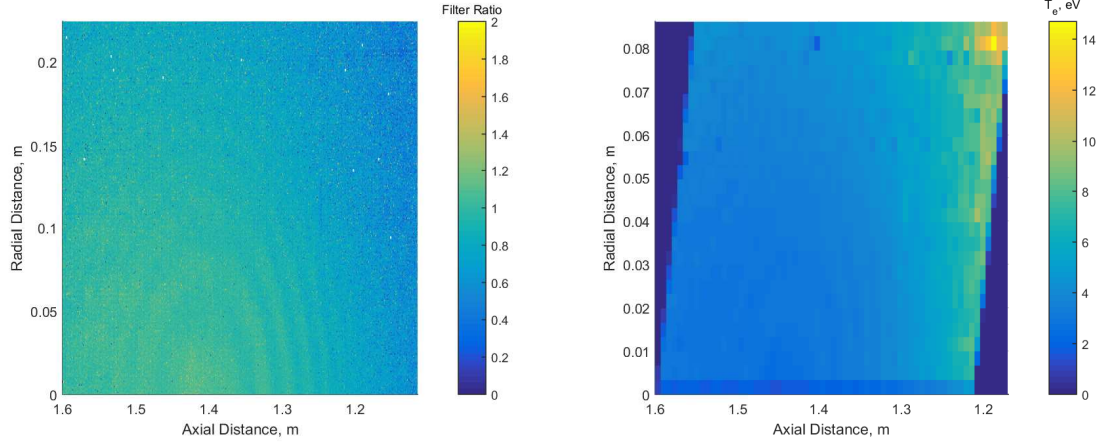


Figure 12. A map of raw 820-nm to 830-nm filter ratios (left) and corresponding smoothed temperatures according to the KCD model (right) for the plume of the X3 inner channel operating near 4 kW. The filter ratio map is not corrected for angular distortion and is not binned, while the temperature map is both corrected and binned. Ratios over 2 were removed from the filter ratio map so that the scaling was meaningful.

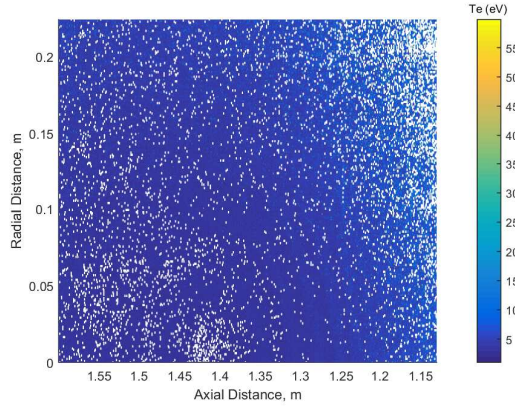


Figure 13. The raw temperature map using the KCD model. This map is uncorrected for angular distortion and all filter ratios that are too high or low for the KCD model are displayed as white. Data is sparse near the top right and bottom left corners, while large swathes are continuous toward the middle of the map.

The spectra for the 820-nm and 830-nm filtered images similarly contain peaks in that vicinity. However, the noisiness of the filtered spectra may skew the prediction of the peak center. Indeed, the unfiltered, 820-nm filtered, and 830-nm filtered peaks based on 10,000 frames were identified as being 4.50 ± 0.43 kHz, 3.94 ± 0.02 kHz, and 4.92 ± 1.80 kHz. The phase of the breathing was also estimated as $-8.68 \pm 0.46^\circ$, $-15.1 \pm 1.7^\circ$, and $10.4 \pm 0.2^\circ$. The uncertainties on these values indicate that over the course of an acquisition the breathing frequency was fairly steady and any deviations were such as to keep the phase steady as well. The uncertainty of these values comes from the width of the spectral peaks to which they correspond according to the Lorentzian fitting scheme mentioned in Section III.

The calculated phases can be used to align the filtered videos and compute the filter ratio, assuming that the phase was nearly constant during the acquisition time. The offset between the two filtered videos was found in this way to be $16 \mu\text{s}$, or roughly one frame. Fig. 16 shows the time-resolved variation of this ratio. Fig. 17 shows the spectrum for the ratio signal. The time-averaged filter ratio for the entire acquisition is 1.12, which corresponds to a KCD electron temperature of 2.40 eV. This value is unreasonably low for the discharge channel plasma, which indicates that KCD model is inappropriate for that region. This may be due to a fundamental breakdown of the model, such as if collisional de-excitation becomes prominent in the discharge channel, or it may be due to the infiltration of unmodeled lines. Investigation with a spectrometer could be used to evaluate the second possibility, and the effectiveness of the model if no intruding lines are

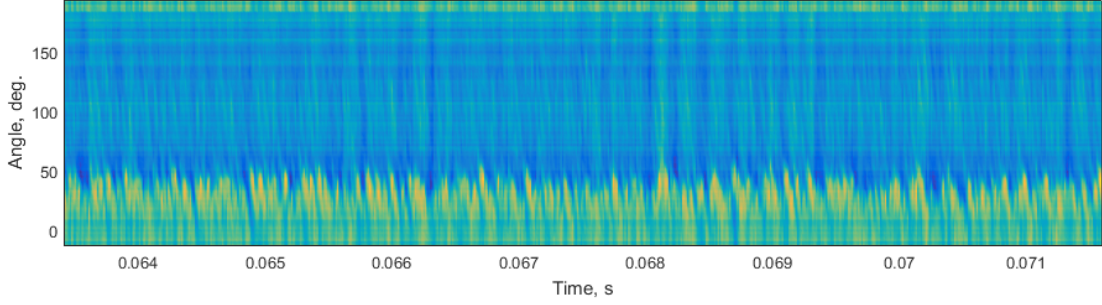


Figure 14. The unfiltered time-resolved intensity map for the inner channel operating near 4 kW. No strong global features are prominent, although turbulent local features do appear at small angles. Some of these features may be artifacts due to reflections off of the viewport and sacrificial glass, while others may be genuine plasma features. Sharp fixed-pattern features (those that are present at all times) are likely camera artifacts.

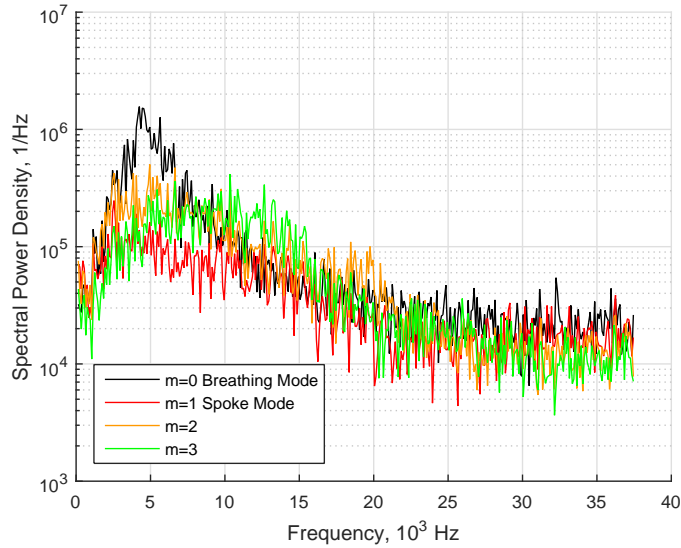


Figure 15. The power spectral density for the unfiltered imaging of the inner channel near 4 kW. A strong breathing mode is present, even though it was not apparent in the intensity map. Higher order modes also appear to be fairly strong, especially the $m=3$ mode. However, the higher order features are so wide that little meaningful analysis can be performed.

found (or if they are accounted for) can be used to evaluate the first possibility.

Although the signal itself appears very noisy, a peak near 5 kHz is apparent in the spectrum, as are half-integer harmonics. The presence of harmonics is not unexpected for the ratio of two periodic signals, although the multitude of them is curious. In any case, strong harmonics are an indication that the two signals are out of phase. This suggests that the spectra are too noisy for the phase correction to be effective, or the phase varies significantly in time. In total, then, a meaningful signal may have been measured, but the lack of strong periodic features and the poor performance of the model means that no usable information can be extracted from the sequential high-speed filtered imaging.

C. Discharge Channel Oscillations

Using the techniques described in Section III, power spectral density curves and intensity maps were produced for each channel in all configurations. These intensity surfaces are included in the appendix as Figs. 20 to 26 for reference when discussing tabulated oscillation properties later. The strong vertical features indicate that the breathing mode was dominant in all conditions. However, spoke-like features in the normalized

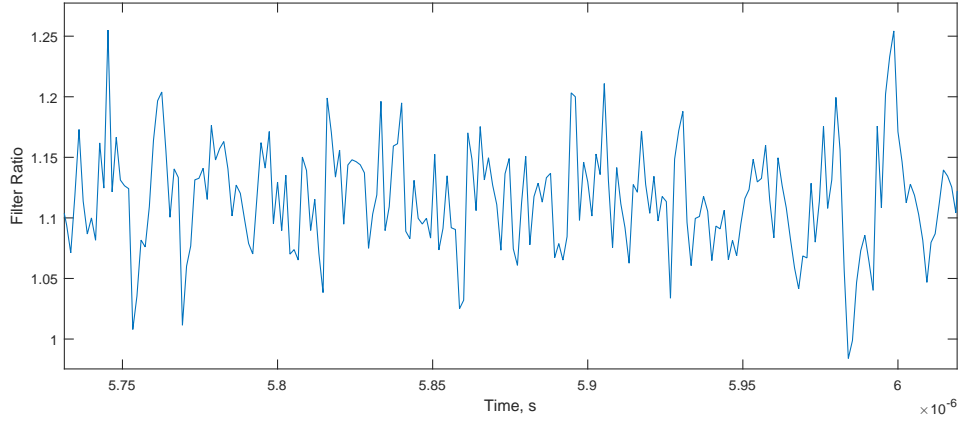


Figure 16. A sample of the time-resolved filter ratio signal. The signal appears to be composed entirely of noise.

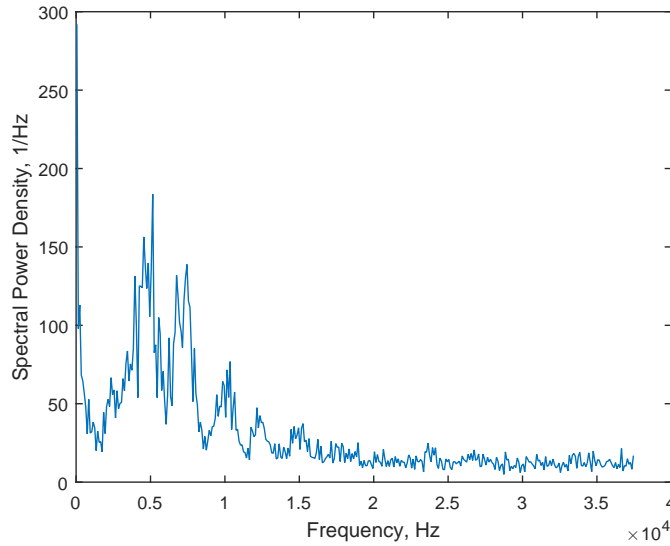


Figure 17. The power spectral density for the filter ratio signal. Considerable power is located at low frequencies, due to the DC offset of the signal. The sharpest AC peaks occur at 5 kHz and every half-integer harmonic.

intensity surfaces can be detected in a few cases, whereas in others turbulent local features are present (and may either be aliased spokes or camera artifacts), and in a few cases there is only noise in the normalized intensity surface. Table 2 qualitatively summarizes the local features present in each, labeling them as artifacts (“art.”), unresolved turbulent features (“turb.”), noise, or spokes (“CCW” or “CW” for spoke propagation direction). The outer channel consistently has observable spokes, despite also experiencing some of the clearest breathing of all channels. This may simply be due to the fact that it was often the brightest channel imaged, so fine features like spokes were easier to distinguish. In total, the lack of defined features in the normalized intensity surfaces indicates that breathing was dominant in all configurations.

Of note is the inner and middle channel case which appears transitional according to its discharge current signals, as discussed in Section IV. The power spectral density from FASTCAM measurements for this case, shown in Fig. 18, indicates that global oscillations dominate at all frequencies for both channels. This suggests that even though it may appear transitional and the transient behavior of the discharge current appears noisy (Fig. 9), most signal spectral power is located in global oscillations. It is possible that the entire image was so dim that spokes, even if they were present, could not be detected by the camera. This

would leave no means to determine the mode other than the discharge current fluctuation amplitude, as will be investigated later.

Table 2. The qualitative local features that can be discerned from the normalized intensity surfaces for all configurations. Local turbulent features are denoted “turb.”, local artifacts are denoted “art.”, and spokes are denoted by their propagation direction.

Case	I	M	O
I	turb.	-	-
M	-	art.	-
O	-	-	CCW
I+M	noise	noise	-
M+O	-	art.	CCW
I+O	noise	-	CCW
I+M+O	noise	art.	art.

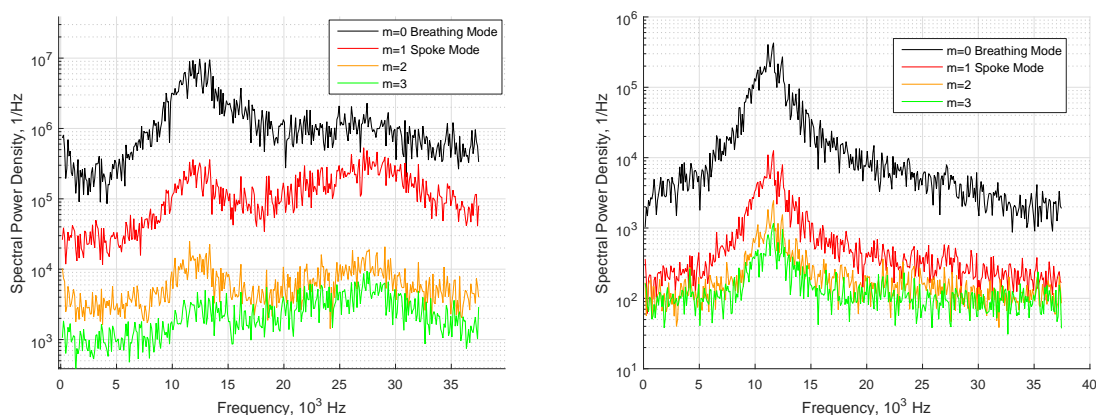


Figure 18. The power spectral density for the inner channel (left) and middle channel (right) when operated in unison. Note that the $m=0$ mode dominates at all frequencies for both channels. There are some higher order features perceptible for the inner channel but they are so broad and weak (relative to $m=0$) that they cannot be taken as a strong indication of spokes.

Given that the thruster was exhibiting the breathing mode in all configurations, comparison between single-, two-, and three-channel operation can be achieved through an examination of the breathing frequency and the width of the breathing spectral peak. Table 3 shows the breathing frequency for each configuration as determined by high-speed image analysis (HIA), with the listed uncertainties ranging the FWHM. Table 3 also shows the same as determined by high-speed discharge current analysis (HCA). The agreement between the two is excellent, with the largest error amounting to only 320 Hz, well within the uncertainty for most cases. The two-channel frequencies differed noticeably from the respective single-channel values, and in general the frequencies approached each other when operated together. For example, the inner channel slowed down when paired with other slower channels, while the middle channel sped up when paired with other faster channels. This agrees with the observations of Hall et al based on the discharge current signal.²⁵ However, it is hard to determine if this change is due to the variation in background pressure between the conditions or if it is related to interaction between the channels.

In the three-channel configuration, breathing frequency convergence occurred with the outer and middle channels in that their frequencies are closer than the single-channel cases. The middle channel generally had a lower frequency than the outer channel in all configurations, but in this case the outer channel sped up slightly and the middle channel sped up significantly. The net effect is frequency convergence, although the means by which it happened is puzzling. Nonetheless, this suggests that there is a strong coupling effect between the outer two channels, regardless of background pressure. On the other hand, the inner channel strongly diverged. There is a weak peak in the inner channel power spectral density, shown in Fig. 19, at the breathing frequency of the other channels, indicating that there is partial coupling. The inner channel frequency is not

a harmonic of the middle/outer frequency, suggesting the channel was breathing very independently aside from the partial coupling. Analytical descriptions of the breathing mode frequency that account for heavy species transport suggest that it is a function of steady state ion and neutral densities in the channel, neutral density at the anode, and the ionization rate coefficient.¹¹ The fact that the breathing frequency is similar for the two outer channels and that the inner channel has weak breathing at that frequency, then, does not seem likely without coupling effects playing a significant role.

Table 3. The center frequencies of the breathing mode for each channel and each configuration based on high-speed discharge current and image analysis.

Case	HCA (kHz)			HIA (kHz)		
	f_I	f_M	f_O	f_I	f_M	f_O
I	14.5±0.4	-	-	14.5±0.4	-	-
M	-	9.99±0.01	-	-	9.99±0.01	-
O	-	-	12.0±0.1	-	-	12.0±0.1
I+M	12.5±1.0	11.3±0.5	-	12.2±0.9	11.4±0.5	-
M+O	-	12.2±0.0	12.2±0.0	-	12.2±0.0	12.2±0.0
I+O	12.9±0.1	-	12.9±5.0	12.9±0.1	-	12.9±0.1
I+M+O	19.9±0.7	12.2±0.8	13.7±0.3	19.5±0.6	12.0±0.8	13.6±0.3

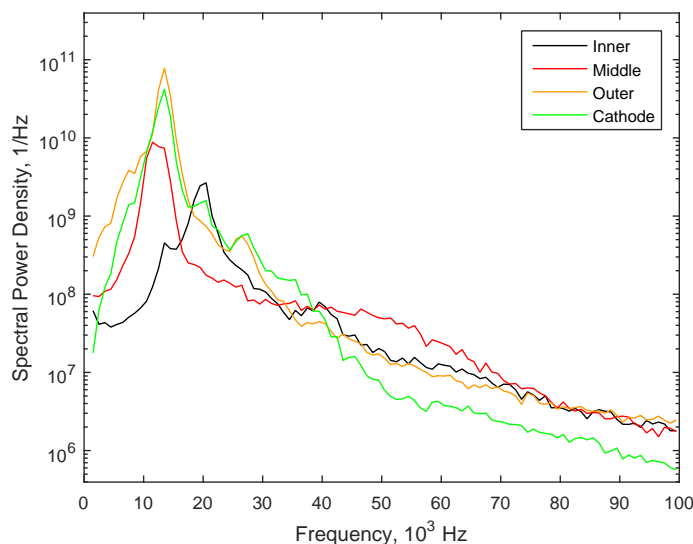


Figure 19. The power spectral density for three-channel operation, binned to 1 kHz. The cathode and outer channel have nearly the same frequency, while the middle channel is slightly lower and broader. The inner channel has a large peak at a higher frequency and a small peak at the cathode frequency.

The phase delays yielded by high-speed image analysis and high-speed discharge current analysis shown in Table 4 did not agree well, with an average difference for all configurations of 6.3°. However, they both show similar trends when comparing phase delays between the two-channel cases and the three-channel case. Namely, the inner channel increased in phase for the inner/middle pair, the outer channel decreased in phase for the outer/middle pair, and the inner channel decreased in phase for the inner/outer pair. The phase delay typically decreased when in three-channel operation. Two exceptions to this trend exist for the high-speed image analysis phase delays, for the inner/middle case where there is a slight increase and for the outer/middle case where the uncertainty of the two-channel configuration phase delay is so large that the phase delay may have increased. For the former exception, it is important to recognize that the inner channel was at a much different frequency than the middle channel, so an average phase delay is not meaningful. Similarly, the middle channel was also at a slightly lower frequency than the outer channel, so the phase delay between the two may also be meaningless. In fact, little useful information can be gleaned from the

phase delays because of this, and so the similarity in trends between the two diagnostics merely indicates that the discharge current and light emission were well-correlated. A more precise means of evaluating signal phase is required to usefully examine phase delays between channels.

Table 4. The phase of the breathing mode for each channel and each configuration based on high-speed discharge current and image analysis.

Case	HCA			HIA		
	θ_{IM}	θ_{OM}	θ_{IO}	θ_{IM}	θ_{OM}	θ_{IO}
I+M	$-10.1\pm 0.3^\circ$	-	-	$1.86\pm 0.39^\circ$	-	-
M+O	-	$23.4\pm 5.8^\circ$	-	-	$26.1\pm 28.0^\circ$	-
I+O	-	-	$11.2\pm 1.0^\circ$	-	-	$24.1\pm 1.3^\circ$
I+M+O	$-1.74\pm 0.30^\circ$	$3.82\pm 0.39^\circ$	$-5.56\pm 0.40^\circ$	$3.27\pm 0.38^\circ$	$-11.3\pm 0.4^\circ$	$14.6\pm 0.5^\circ$

The breathing RMS amplitude also varies for a given channel between the different configurations. Table 5 shows the RMS amplitude for each configuration. Since discharge current was kept constant, these amplitudes should be comparable between configurations. However, the wildly varying background pressure may have influenced the mode, which would in turn impact the RMS amplitude. In this way, any observable trends cannot entirely be trusted to be independent of pressure effects. In any case, there do not appear to be any strong trends in the discharge current fluctuations. Whereas the inner channel has its largest fluctuations when part of the three-channel configuration, the middle and outer channels vary sporadically. It is likely that the strength of these fluctuations are dependent on a combination of many operating parameters, such that simply operating in the breathing mode — as the thruster was in all configurations — is not enough to specify the strength of fluctuations more than with a broad range. In general, the fluctuation amplitudes were small, most being more characteristic of the spoke mode than the breathing mode. In total, the low fluctuation amplitudes provide evidence that, even though global oscillations were dominant, most operating conditions may have been near the mode transition point.

It was previously noted that the inner/middle case may have been transitional given the noisiness of its discharge current signal and how weak it's breathing oscillations were. The RMS amplitude for the middle channel in this case is especially low, well into the range typically associated with spokes. However, both channels in this configuration showed only noise in their intensity surfaces. This suggests that the thruster was at least transitioning between modes in this case, although the complete absence of spokes still suggests that it was closer to the breathing mode than the spoke mode. Alternatively, if the spokes were too dim to be detected by the camera, this configuration may have been closer to the spoke mode.

It is interesting to note that the inner channel had higher relative fluctuations than the other channels in the inner and middle two-channel configuration (as discussed previously) and the three-channel configuration. For the latter case, this means that not only was the inner channel breathing much faster than the other channels, it was breathing much harder. In this sense, the high-speed behavior of the inner channel was very different from the others, even though they were qualitatively exhibiting the same mode.

Table 5. The discharge current RMS amplitude for all channels and configurations. Fluctuation currents are shown on the left and relative fluctuations are shown on the right.

Case	\tilde{I}_I (A)	\tilde{I}_M (A)	\tilde{I}_O (A)	Case	$(\tilde{I}/I_d)_I$	$(\tilde{I}/I_d)_M$	$(\tilde{I}/I_d)_O$
I	3.06	-	-	I	22.7%	-	-
M	-	7.51	-	M	-	23.9%	-
O	-	-	17.40	O	-	-	31.7%
I+M	1.66	1.17	-	I+M	12.4%	3.71%	-
M+O	-	5.03	20.45	M+O	-	16.0%	37.3%
I+O	1.16	-	17.47	I+O	8.73%	-	31.6%
I+M+O	3.93	6.71	15.19	I+M+O	28.9%	20.8%	27.6%

VI. Conclusion

The investigation detailed in this paper explored the potential for xenon optical emission spectroscopy with a high-speed camera for the purpose of characterizing Hall thruster oscillations. Additionally, the oscillations present in a nested Hall thruster were examined, and a comparison between single-channel, two-channel, and three-channel operation was made. This work was motivated by the need for a better understanding of Hall thruster oscillations, which are known to depend on operating conditions — many of which vary between ground testing and actual flight applications — and can strongly affect performance.

The KCD Xe I collisional-radiative model was used to predict time-averaged electron temperatures in a Hall thruster plume. This required imaging the plume with two filters, centered at 820 nm and 830 nm. The ratio of the sensor signal with these filters could be used to estimate electron temperature. The noisiness of the sensor made the data sparse but there was still surprising agreement between the predicted temperatures and those yielded by a Langmuir probe. Although this one-point comparison does not speak to the accuracy of the entire temperature map produced with the OES method — and indeed the map seems to lose accuracy in some regions — it does indicate that emission spectroscopy is possible with a high-speed camera.

Filtered high-speed imaging of the discharge channel was also attempted. Because the imaging was performed on time scales at which high-speed oscillations can be detected, the videos captured with different filters had to be phase adjusted. This was done by identifying the breathing mode frequency for each video and then calculating the phase associated with the breathing mode power spectral density peak. A time-resolved filter ratio signal was produced this way and the signal showed periodicity at the breathing mode frequency, but the presence of harmonics also suggested that there was still a phase offset between the two signals. Additionally, the time-averaged filter ratio led to predictions of a very low temperature, which is unreasonable. This suggests that the traditional KCD model is inapplicable to the discharge channel, as suspected, and that unmodeled emission lines may be infiltrating the wavelength ranges of interest.

The center frequency and phase for breathing mode oscillations in a nested Hall thruster was determined for all 30 kW, 300 V channel configurations. Breathing frequencies generally approached each other in two-channel operation, but the influence of background pressure makes it difficult to determine if this is really a coupling effect. For the three-channel case, the inner channel had a noticeably different breathing frequency, although evidence of partial coupling was observed. This suggests that channel coupling strongly influences the discharge channel instability mode. The breathing phases also appeared to converge for three-channel operation, but the difference in breathing frequencies suggests this trend is coincidental. Finally, fluctuation amplitudes did not change consistently between configurations, implying that other operation parameters were affecting the behavior of the thruster for each case.

Appendix

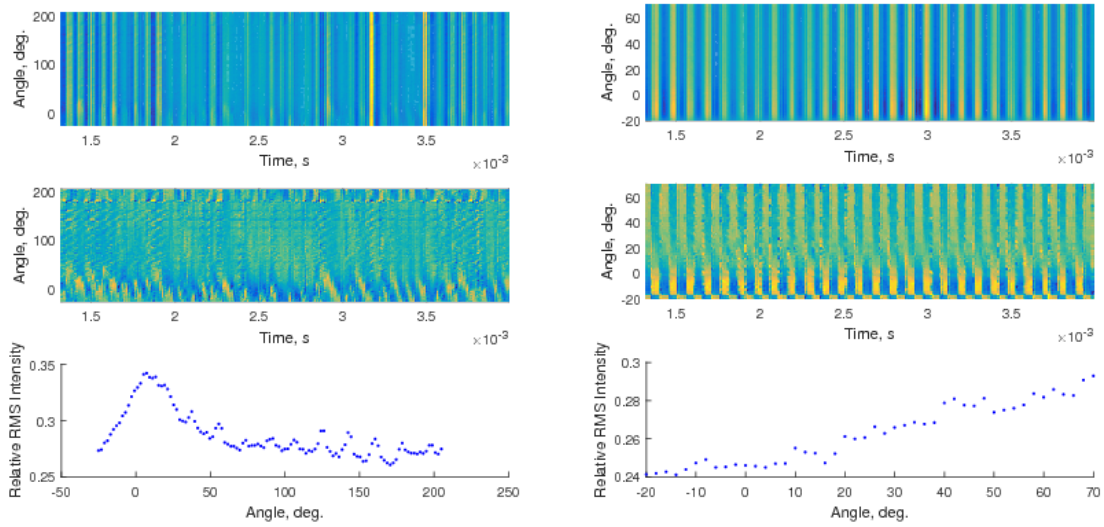


Figure 20. The intensity surface (top), spatially-normalized intensity surface (middle), and spatial fluctuation distribution (bottom) for the inner channel alone (left) and the middle channel alone (right).

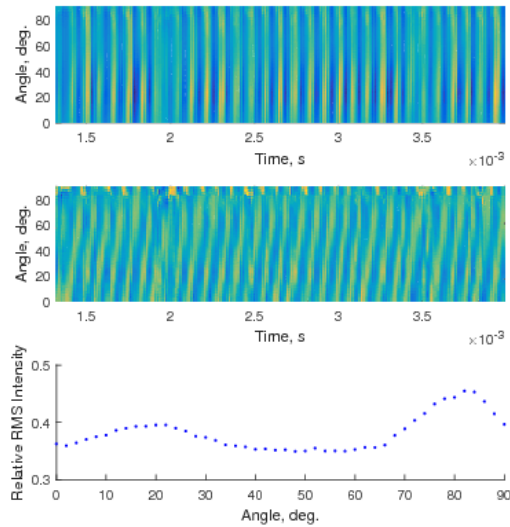


Figure 21. The intensity surface (top), spatially-normalized intensity surface (middle), and spatial fluctuation distribution (bottom) for the outer channel alone.

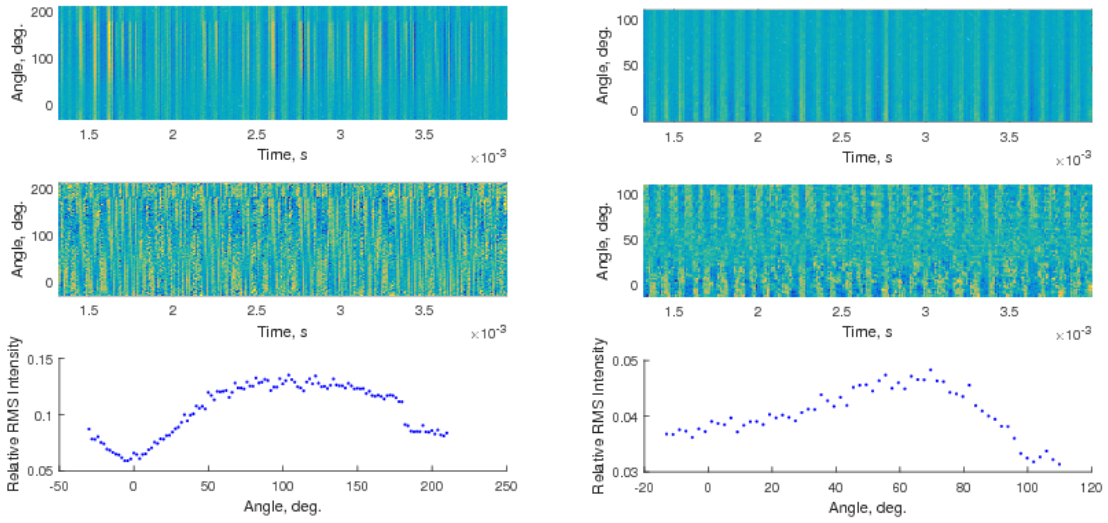


Figure 22. The intensity surface (top), spatially-normalized intensity surface (middle), and spatial fluctuation distribution (bottom) for the inner channel (left) and the middle channel (right) for simultaneous operation.

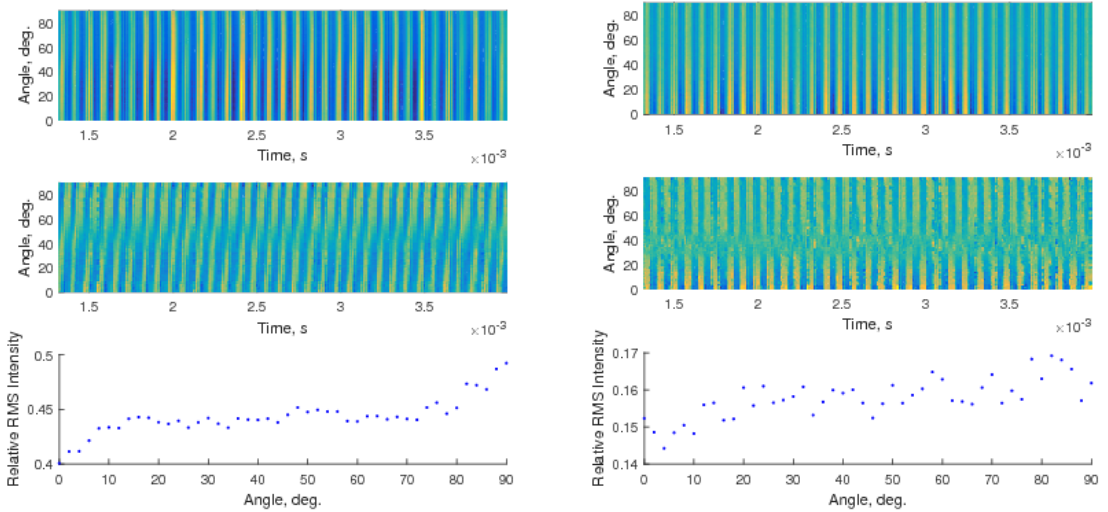


Figure 23. The intensity surface (top), spatially-normalized intensity surface (middle), and spatial fluctuation distribution (bottom) for the outer channel (left) and the middle channel (right) for simultaneous operation.

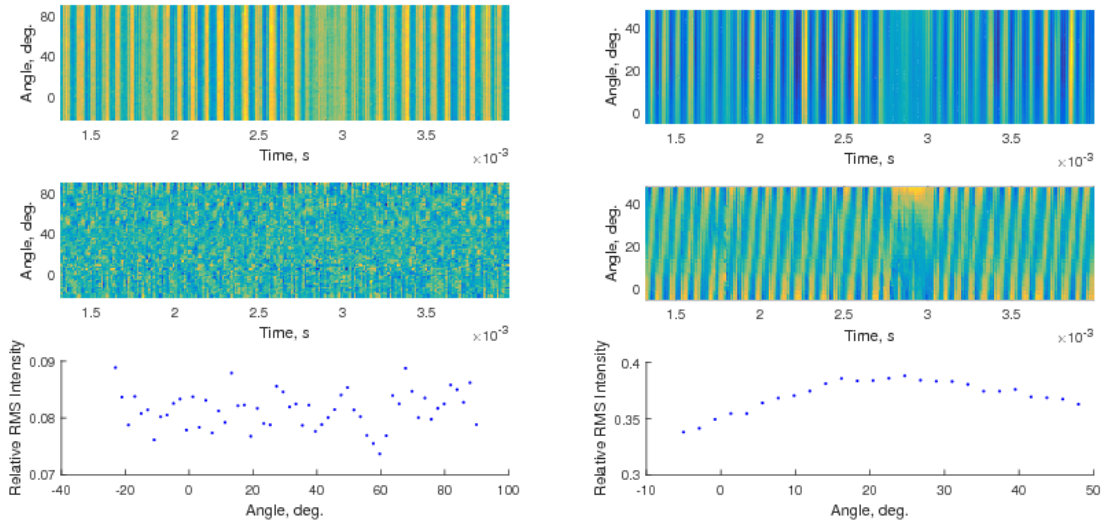


Figure 24. The intensity surface (top), spatially-normalized intensity surface (middle), and spatial fluctuation distribution (bottom) for the inner channel (left) and the outer channel (right) for simultaneous operation.

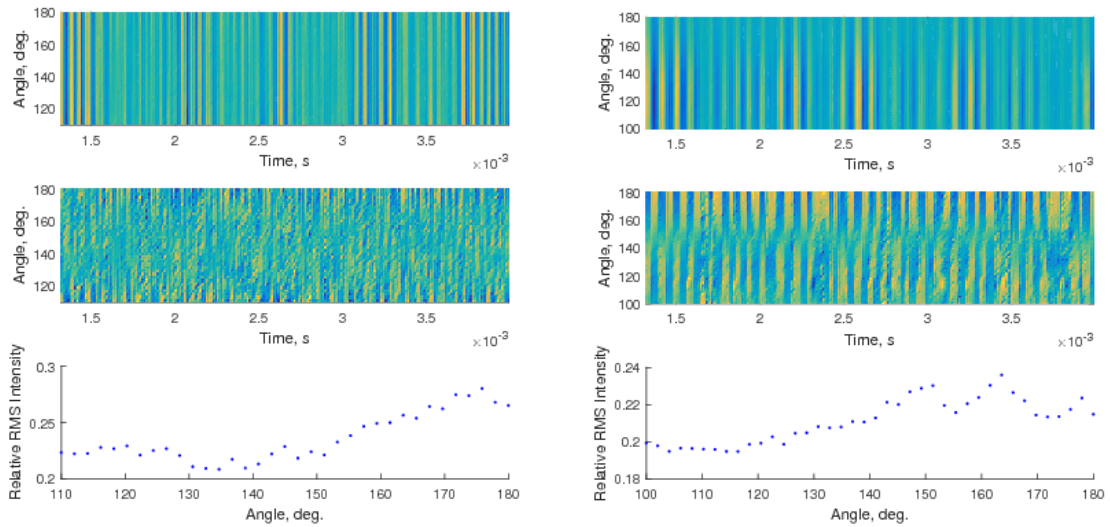


Figure 25. The intensity surface (top), spatially-normalized intensity surface (middle), and spatial fluctuation distribution (bottom) for the inner channel (left) and the middle channel (right) for three-channel operation.

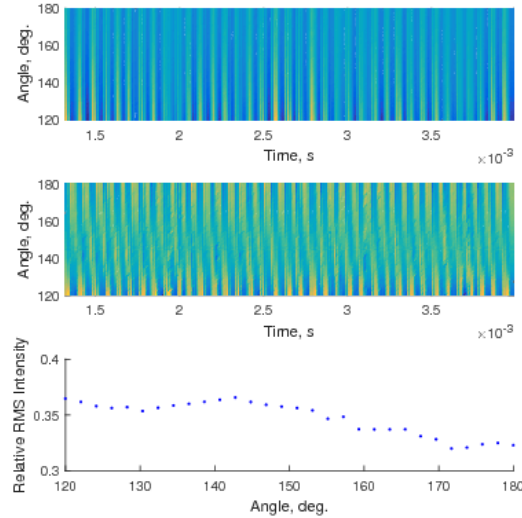


Figure 26. The intensity surface (top), spatially-normalized intensity surface (middle), and spatial fluctuation distribution (bottom) for the outer channel for three-channel operation.

Acknowledgments

The author (E. Dale) would like to acknowledge the support provided for this work by NASA Space Technology Research Fellowship (NSTRF) grant NNX14AL65H. He would also like to thank his NSTRF mentor Dr. Wensheng Huang for his contributions to the work described in this paper.

References

- ¹“Low Earth Orbit Spacecraft Charging Design Handbook,” NASA-HDBK-4006, National Aeronautics and Space Administration, Washington, DC, 2007.
- ²Walker, J.A., Frieman, J.D., and Walker, M.L.R., “Hall Effect Thruster Electrical Interaction with a Conductive Vacuum Chamber,” *50th AIAA/ASME/SAE/ASEE Joint Propulsion Conference*, Cleveland, OH, July 28-30, 2014.
- ³Sekerak, M.J., Longmier, B.W., Gallimore, A.D., Brown, D.L., Hofer, R.R., and Polk, J.E., “Mode Transitions in Hall Effect Thrusters,” *49th AIAA/ASME/SAE/ASEE Joint Propulsion Conference*, San Jose, CA, July 14-17, 2013.
- ⁴Choueiri, E. Y., “Plasma oscillations in Hall thrusters, *Physics of Plasmas*, Vol. 8, No. 4, 2001, pp. 1411.
- ⁵Morozov, A.I., Epsinchuck, Y., Kapulkin, A.M., Nevrovskii, A., and Smirnov, V.A., *Soviet Physics – Technical Physics*, Vol. 17, 482, 1972.
- ⁶Epsinchuck, Y., and Tilinin, G., *Sov. Phys. Tech. Phys.*, Vol. 21, pp. 417, 1976.
- ⁷Boeuf, J.P., and Garrigues, L., *Journal of Applied Physics*, Vol. 84, pp. 3541-3554, 1998.
- ⁸Darnon, F., Lyszyk, M., and Bouchoule, A., “Optical Investigation on Plasma Oscillations of SPT Thrusters,” *American Institute of Aeronautics and Astronautics*, Washington, DC, 1997.
- ⁹Fife, J., Martinez-Sanchez, M., and Szabo, J., “A Numerical Study of Low-Frequency Discharge Oscillations in Hall Thrusters,” *American Institute of Aeronautics and Astronautics*, Washington, DC, 1997.
- ¹⁰Barral, S., and Ahedo, E., “Low-frequency model of breathing oscillations in Hall discharges, *Physical Review E*, Vol. 79, No. 4, 2009.
- ¹¹Hara, K., Sekerak, M., Boyd, I.D., and Gallimore, A.D., “Perturbation analysis of ionization oscillations in Hall effect thrusters,” *Physics of Plasmas*, Vol. 21, 2014.
- ¹²Hara, K., “Development of Grid-Based Direct Kinetic Method and Hybrid Kinetic-Continuum Modeling of Hall Thruster Discharge Plasmas,” Ph.D. dissertation, Department of Aerospace Engineering, University of Michigan, Ann Arbor, MI, 2015.
- ¹³Sekerak, M.J., Longmier, B.W., Gallimore, A.D., Brown, D.L., Hofer, R.R., and Polk, J.E., “Azimuthal Spoke Propagation in Hall Effect Thrusters,” *33rd International Electric Propulsion Conference*, Washington D.C., October 6-10, 2013.
- ¹⁴Sekerak, M.J., Longier, B.W., Gallimore, A.D., Huang, W., Kamhawi, H., Hofer, R.R., Jorns, B.A., and Polk, J.E., “Mode Transitions in Magnetically Shielded Hall Effect Thrusters,” *50th AIAA/ASME/SAE/ASEE Joint Propulsion Conference*, Cleveland, OH, July 28-30, 2014.
- ¹⁵Jorns, B. A. and Hofer, R. R., “Plasma oscillations in a 6-kW magnetically shielded Hall thruster, *Physics of Plasmas*, Vol. 21, No. 5, pp. 053512, 2014.

- ¹⁶Liang, R., "The Combination of Two Concentric Discharge Channels into a Nested Hall-Effect Thruster," Ph.D. dissertation, Department of Aerospace Engineering, University of Michigan, Ann Arbor, MI, 2013.
- ¹⁷McDonald, M.S., Sekerak, M.J., Gallimore, A.D., and Hofer, R.R., "Plasma Oscillation Effects on Nested Hall Thruster Operation and Stability," *IEEE Aerospace Conference*, Big Sky, MT, March 2-9, 2013.
- ¹⁸Florenz, R.E., "The X3 100-kW Class Nested-Channel Hall Thruster: Motivation, Implementation and Initial Performance," Ph.D. dissertation, Department of Aerospace Engineering, University of Michigan, Ann Arbor, MI, 2014.
- ¹⁹Manzella, D.J., "Stationary Plasma Thruster Plume Emissions," *23rd International Electric Propulsion Conference*, Columbus, OH, 1993, Report No. IEPC-93-097, 2003.
- ²⁰N. B. Meezan, J. W. A. Hargus, D. P. Schmidt, and M. A. Cappelli, "Optical Study of Anomalous Electron Transport in a Laboratory Hall Thruster," *35th AIAA/ASMFISAFIASEE Joint Propulsion Conference*, Los Angeles, CA, 1999.
- ²¹Karabadzhak, G., "Improvement of Optical Diagnostic Technique for a Xenon Operating Hall Effect Thruster," *4th International Spacecraft Propulsion Conference*, Chia Laguna, Sardinia, Italy, June 2-9, 2004.
- ²²Karabadzhak, G.F., Chiu, Y., and Dressler, R.A., "Passive Optical Diagnostic of Xe-propelled Hall Thruster, II. Collisional-Radiative Model," *Journal of Applied Physics* 99, 2006.
- ²³Dressler, R.A., Chiu, Y., Zatsarinny, O., Bartschat, K., Srivastava, R., and Sharma, L., "Near-infrared collisional radiative model for Xe plasma electrostatic thrusters: the role of metastable atoms," *Journal of Physics D: Applied Physics*, Vol. 42, 2009.
- ²⁴Gonzales, A.E., Koo, J.W., and Hargus, W.A. Jr., "Comparison of Numerical and Experimental Time-Resolved Near-Field Hall Thruster Plasma Properties," *IEEE Transactions on Plasma Science*, Vol 42, No , 2014.
- ²⁵Hall, S., Florenz, R.E., and Gallimore, A.D., "Implementation and Initial Validation of a 100-kW Class Nested-channel Hall Thruster," *50th AIAA/ASME/SAE/ASEE Joint Propulsion Conference*, Cleveland, OH, July 28-30, 2014.
- ²⁶Dankanich, J.W., Walker, M., Swiatek, M.W., and Yim, J.T., "Recommended Practice for Pressure Measurements and Calculation of Effective Pumping Speeds during Electric Propulsion Testing," *33rd International Electric Propulsion Conference*, Washington D.C., October 6-10, 2013.
- ²⁷McDonald, M. S., and Gallimore, A. D., "Rotating Spoke Instabilities in Hall Thrusters," *IEEE Transactions on Plasma Science*, Vol. 39, pp. 2952-2953, 2011.
- ²⁸Jung, R.O., Stone, T.E., Boffard, J.B., Anderson, L.W., and Lin, C.C., "Electron-impact excitation cross sections from the xenon J=2 metastable level," *Physical Review A*, Vol. 72, 2005.